Melt-affected Ocean Crust and Uppermost Mantle near Hawaii

- Clues from Ambient-Noise Phase Velocity and Seafloor

Compliance

A.K. Doran¹ and G. Laske

¹ Cecil H. and Ida M. Green Institute of Geophysics and Planetary Physics, 0225, La Jolla, U.S.A.

SUMMARY

We present models of crustal and uppermost mantle structure beneath the Hawaiian Swell and

surrounding region. The models were derived from ambient-noise intermediate-period Rayleigh-

wave phase velocities and from seafloor compliance that were estimated from continuous seis-

mic and pressure recordings collected during the Hawaiian Plume-Lithosphere Undersea Mantle

Experiment (PLUME). We jointly inverted these data at the locations of over 50 ocean-bottom

instruments, after accounting for variations in local bathymetry and sediment properties. Our

results suggest that the crystalline crust is up to 15 km thick beneath the swell and up to 23

km thick closer to the islands. Anomalously thick crust extends toward the older seamounts,

downstream of Hawaii. In a second region, anomalies immediately to the south of Hawaii may

be associated with the leading edge of the shallow Hawaiian magma conduit. In a third region,

thickened crust to the immediate west of Hawaii may be related to Cretaceous seamounts. Low

seismic velocities identified in the uppermost mantle to the northeast of Hawaii may be linked

to the Molokai Fracture Zone and may be manifest of complex non-vertical pathways of melt

through the upper lithosphere. Velocity anomalies decrease in amplitude towards the surface,

2 A.K. Doran

suggesting that melt becomes focused into conduits at depths between 20 and 40 km that escape the resolution capabilities of our dataset.

Key words: composition and structure of the oceanic crust, hotspots, surface waves and free oscillations, seismic interferometry, seismic tomography

1 INTRODUCTION

The Hawaiian hotspot has long been hypothesized to be the surface expression of a deep-rooted mantle plume (e.g., Wilson 1963). Although many aspects of plume theory remain contested, recent analyses of diverse geophysical observations have provided evidence that a thermochemical plume extends from the base of the mantle (e.g., French & Romanowicz 2015), through the lower mantle and the transition zone (e.g., Ritsema & Allen 2003; Wolfe et al. 2009, 2011; Cheng et al. 2015; Agius et al. 2017), and into the lithosphere beneath Hawaii (e.g., Constable & Heinson 2004; Laske et al. 2007, 2011). Contrary to the original theory of a purely vertical mantle conduit (e.g., Morgan 1971; Phipps Morgan et al. 1995), the upwelling mantle melt appears to travel through complex non-vertical pathways. While ascending east of the islands below the mantle transition zone (Wolfe et al. 2009), the plume intersects the lithosphere to the west of the active volcanism on the island of Hawaii (Li et al. 2004; Laske et al. 2011; Rychert et al. 2013). Regional seismic tomographic studies have identified low seismic velocities (suggesting 1-2% partial melt and elevated temperatures) west of the islands at depths of 60 km and greater (Laske et al. 2007, 2011), but have lacked resolution in the uppermost lithosphere and crust to image shallower structure. Characterizing the melt conduit through the upper lithosphere and crust remains a missing link in understanding the Hawaiian hotspot, the mechanics of mantle dynamics, mantle melt transport, and the thermal evolution of the mantle.

In return, the variable nature of the oceanic crust beneath and surrounding the Hawaiian Islands has been an impediment to high-fidelity images of the lithosphere. The crystalline crust around Hawaii thickens from typical values of approximately 6 km far from the islands (e.g., Watts et al. 1985; Lindwall 1991) to 20 km or greater beneath the islands (e.g., ten Brink & Brocher 1987; Watts & ten Brink 1989; Zucca et al. 1982; Wölbern et al. 2006; Leahy et al. 2010). Much of the thickened crust has been proposed to be the result of magmatic underplating, with seismic velocities and densities intermediate between mantle and crustal values and potentially contributing to the bathymetric uplift surrounding Hawaii (e.g., Leahy & Park 2005; Leahy et al. 2010). In addition, marine sediments vary significantly in both thickness and elastic properties surrounding the islands, ranging from less than 100 meters at some points on the Hawaiian Swell to over 2 km within the Hawaiian Moat (e.g., Rees et al. 1993; Leslie et al. 2002; Doran & Laske 2019). Not accounting for effects

that such variations impose on broadband seismic data and other geophysical observables (e.g., Marone & Romanowicz 2007) almost certainly leads to biased models of the underlying crust, and possibly the mantle beneath.

The Hawaiian Plume-Lithosphere Undersea Melt Experiment (PLUME, Laske et al. 2009), an amphibious multi-year deployment consisting of 10 land seismometers and over 70 broadband ocean-bottom seismometers (OBSs) surrounding the Hawaiian islands (Fig. 1), provided a unique dataset to study the architecture of the Hawaiian hotspot (Wolfe et al. 2009, 2011; Leahy et al. 2010; Laske et al. 2011; Collins et al. 2012; Rychert et al. 2013; Agius et al. 2017). For this study, we analyzed continuous seismic data to measure Rayleigh wave phase velocities at discrete periods between 16 and 24 seconds from cross-correlations waveforms of ambient seismic noise (Fig. 2). These data were ultimately incorporated with measurements of seafloor compliance from pressure records in an inversion for crustal and uppermost mantle structure. Seafloor compliance is the transfer function between pressure variations imposed by passing ocean infragravity waves and ground movement in response to that. Our seafloor compliance measurements made for PLUME were previously described by Doran & Laske (2019). Phase velocities are primarily sensitive to structure in the lower crust and uppermost mantle, while compliance data are most sensitive to the upper crust and sediments (Fig. 3). Important of note here is that seafloor compliance is site-specific and so provides in-situ information on structure beneath each OBS site. On the other hand, dispersion curves obtained from the cross-correlation waveforms as shown in Fig. 2 are path-averaged dispersion curves. The collection of all two-station dispersion curves then is the basis of subsequent tomographic inversions for period-dependent dispersion maps. At each of the OBS sites, a 'local dispersion curve' can then be reconstructed from the dispersion maps and subsequently be used in a joint inversion with seafloor compliance for local depth-dependent structure.

Our results suggest that the oceanic crystalline crust in the study area is approximately 6 km thick under about half of our OBS sites but can be up to to 15 km thick beneath the swell surrounding the island chain, and up to 23 km thick toward the islands and to the immediate south and west of the island of Hawaii. Crustal velocities vary on the order of several percent over the array, with lower velocities adjacent to the islands. A wide low-velocity region in the uppermost mantle extends east-west across the island chain at depths up to 40 km, corresponding to several percent of melt or elevated temperatures. Pronounced low velocities northeast of Hawaii may be associated with the Molokai Fracture Zone. The mantle velocity anomalies decrease towards the surface, suggesting that melt may become geographically focused beneath Hawaii at these depths, and at scales smaller than our surface wave measurements can resolve.

2 DATA AND DATA PROCESSING

2.1 Data Types and Sensitivities

Seafloor compliance is a measure of the deformation of the oceanic crust in response to loading from infragravity waves at periods longer than \geq 30 seconds (e.g., Crawford et al. 1991; Crawford & Webb 2002; Doran & Laske 2016). The applicable period range is limited by the water depth at short periods. The PLUME OBSs were deployed at depths 4400 meters or greater, so compliance observations are possible at periods longer than about 60 seconds. At long periods, uncertainties in the instrument responses, particularly for the pressure sensor, limits reliable compliance observations to periods shorter than about 140 seconds. Compliance data in this period range primarily sample the structure of the upper crust (Fig. 3), including marine sediments if present, and are particularly sensitive to regions of low shear velocity (Vs). The compliance data presented here have been previously described by Doran & Laske (2019), where they were jointly inverted with Ps converted phases originating at the sediment-bedrock interface for detailed sedimentary velocity and density profiles. With sediment properties determined reliably, but because seafloor compliance also carry great sensitivity to crustal shear velocities, a joint analysis with phase velocity measurements allows us to characterize the crust and uppermost mantle with greater confidence than using dispersion curves alone.

Frequency-dependent surface wave group and phase velocity measurements between two stations are regularly used to constrain Earth structure (see, e.g., Romanowicz 2002, for a review). Recovering dispersion information from ambient noise records has progressed beyond infancy and is now a routine method of imaging the structure of both continental and oceanic lithosphere (e.g., Lin et al. 2006; Bensen et al. 2007; Harmon et al. 2007; Campillo & Roux 2015). Much like the analysis of teleseismic surface waves, ambient noise yields path-averaged dispersion curves that accumulate information on structural heterogeneity along the travel path between two stations. The frequency-dependence provides sensitivity to structure at depth. We assembled phase velocities in the period range between 16 and 24 seconds. Insufficient levels of coherency limit our ambient-noise analysis at long periods, while enhanced sensitivity to variations in water depth impose limits at short periods, as documented below. At periods used here, phase velocities are sensitive to the elastic structure of the crust and uppermost mantle (Fig. 3), with longer periods sampling deeper structure. Since the kernels for Vp increase toward the surface, we should expect an increasing sensitivity to changes in the ocean water layer as period decreases (e.g., Harmon et al. 2007). PLUME OBSs were deployed at seafloor depths between 4400 and 5800 meters. Fig. 4 displays the expected contribution to phase velocity anomalies resulting from only bathymetric variations across the array. While the effects of changes in bathymetry on phase velocity tend to be on the order of 1\% or less at periods of 20 seconds and longer, effects at periods shorter than 18 seconds can be several percent or more (see also Fig. S1). The impacts of bathymetric variations on seafloor compliance are practically insignificant in comparison. Our local starting models for the inversion of ambient noise dispersion data for depth structure therefore must properly represent local water depths.

The compliance kernels in Fig. 3 peak at much shallower depth than the ambient noise kernels, so a casual reader may infer that we could follow a top-down approach where we invert the compliance data for shallow crustal structure first. This model would then be used as starting model in a subsequent inversion of the ambient-noise data for deeper crustal and uppermost mantle structure. However, the kernels for compliance and ambient noise, even as shown here, are not orthogonal, and so the data are not independent. To get a better feel for the various dependencies, we performed targeted forward modeling where a single parameter is changed and effects are evaluated (Fig. S1). In the period range considered here, phase velocity is insignificantly sensitive to variations in sediment velocities. The thickness of thin sediments, up to 200 m, can have a small effect at shorter periods but is also insignificant. On the other hand, seafloor compliance changes on the order of a large multiple of measurement error bars. An independent inversion of seafloor compliance data for sediment structure as done by Doran & Laske (2019) is therefore indicated. The situation changes when the crystalline crust is modified as both seafloor compliance as well as phase velocity are affected significantly. Therefore, a top-down approach separating the treatment of compliance and ambient-noise data for upper and lower crystalline crust is no longer justified. Farther down yet, changes in crustal thickness by 3 km impact phase velocities but leave compliance largely unaffected. And not lastly, phase velocities are dramatically affected by changes in uppermost mantle velocities, while compliance remains unaffected. Magmatic underplating proposed beneath the Hawaiian islands and the surrounding area (Leahy et al. 2010) should therefore be detectable by the phase velocity data. To summarize, while the sensitivity of seafloor compliance may peak in the upper crust, significant sensitivity into the lower crust remains, particularly for longer periods. We therefore prefer a joint inversion of seafloor compliance and phase velocity for structure in the entire crustal column as well as uppermost mantle as opposed to two separate inversions, one of seafloor compliance for shallow crustal structure and then phase velocity for deeper structure.

2.2 PLUME Instrumentation and Data Assembly

The PLUME field campaign included two year-long deployments of 3-component wideband and broadband OBSs at over 60 seafloor sites with an array aperture of over 1000 km (Fig. 1; Laske et al. 2009). The campaign was enhanced by the concurrent operation of 10 land stations distributed over the Hawaiian islands. All sites recorded seismic ground motion on three components. The majority of the OBSs were provided by Woods Hole Oceanographic Institute (WHOI) and contained Güralp CMG-3Ts (long-period corner period at

6 A.K. Doran

120 seconds). The remaining instruments were provided by Scripps Institution of Oceanography (SIO), of which the PLUME phase 1 instruments contained Nanometrics Trillium 40 wide-band seismometers (corner period at 40 s) and the PLUME phase 2 instruments contained Nanometrics Trillium 240 broadband seismometers (corner period at 240 s). All OBSs recorded pressure changes on Cox-Webb differential pressure gauges (DPGs; Cox et al. 1984). The ten land stations were equipped with Wielandt-Streckeisen STS-2s (corner period 120 seconds). The dispersion measurements in this study rely on vertical seismometer data, while seafloor compliance was derived from the normalized transfer functions between vertical displacement and seafloor pressure. Horizontal seismometer records were utilized to improve vertical signal-to-noise ratios for both measurement types (e.g., Crawford et al. 2006).

Seafloor compliance data are crucially dependent on accurate instrument response information to determine absolute values. While the seismometer responses should be well constrained, the response of individual DPGs can vary significantly from the nominal response in both gain and corner frequency (Doran et al. 2019). Especially the latter affects data at periods of 60 seconds and longer. We therefore calibrated the response gain of individual DPGs in situ during post processing of the data using the method of Zha & Webb (2016). To gauge horizontal ground motion, the geographic orientations for the horizontal seismometer components were taken from Doran & Laske (2017). Station details are provided in Table S1.

We computed ambient noise cross-correlation functions between station pairs, following closely the method of Bensen et al. (2007). We used data sampled at 1 sps where available directly (WHOI instruments), or we downsampled data to 1 sps (SIO instruments from 31.25 sps, land stations from 20 sps). We band-pass filtered the data between 3 and 100 seconds, removed the nominal instrument response, removed the tilt signal (Bell et al. 2015; Doran & Laske 2019), and applied one-bit normalization and spectral whitening (e.g., Lecocq et al. 2014). We computed cross-correlation functions using 24-hour streams of continuous data, windowed with a boxcar taper. We subsequently stacked the daily correlograms to improve the signal-to-noise ratio. All available OBSs and land stations were included in our analysis to assemble a high-quality database of 484 symmetric waveforms, after careful data vetting (Fig. 2). Sorted by two-station distance, a move-out is clearly visible. As distance increases, a significant delay with respect to our SWELL starting model (Laske et al. 2007) becomes apparent and indicates that at least some portions of the crust and uppermost mantle in the area exhibit anomalously low structural velocities. From these waveforms, frequency-dependent phase velocities were measured for each two-station pair following the method of Ekström et al. (2009), itself based on the formulation of Aki (1957). In this approach, the zero-crossings of the real part of the cross-spectrum (computed from the cross-correlation waveforms) are associated with zeros of a Bessel function of the first kind, allowing us to derive phase velocities at discrete periods. The resulting dispersion curves were then resampled at nine periods desired for this study, between 16 and 24 seconds. We obtained internally consistent phase velocity curves with high signal-to-noise ratios along all 484 paths. Fig. 5a provides a map illustration of the sets of two-station path-averaged phase velocities for two select periods.

It is important to emphasize that these initial phase velocities are path-averaged and that tomographic inversions are needed to retrieve local period-dependent phase velocities and, ultimately, structure as function of depth, our final goal. In principle, this can be achieved in two approaches but each involves two steps. One approach constrains crustal and mantle structure by inverting each two-station dispersion curve for path-averaged shear velocity as a function of depth. A subsequent set of tomographic inversions relates these functions to maps of shear velocity at fixed depth, and ultimately to 3-dimensional structure. However, bathymetry, sediment thickness, and crustal structure vary significantly over the array. Prior to a depth inversion, bathymetry and sediment structure would have to be integrated for each two-station path which may be rather impractical. For example, the sediment structure is known only at the OBS sites (Doran & Laske 2019) but not in between, and interpolations between stations may introduce artifacts. It is therefore more straightforward to perform map inversions of phase velocity first, and then invert phase velocities at each OBS site for a local velocity-depth profile, after re-assembly of local dispersion curves from the resulting maps (for a detailed discussion, see Laske et al. 2011). In our study, we would combine local phase velocity with the compliance data in a joint inversion for depth structure. The advantage of this approach also is that effects of bathymetry and sediment structure can easily be implemented in the starting model at each site.

We inverted the path-averaged dispersion curves for maps of Rayleigh-wave phase velocities at all nine periods between 16 and 24 seconds. The resulting maps for two periods are shown in Fig. 5b. For each period, an inversion solved for a phase velocity map defined in 13 x 13 one-degree cells using second-derivative smoothing in an Occam inversion (Constable et al. 1987; Laske et al. 2011). Here, a regularization parameter, μ , balanced the data misfit, χ^2 , against the roughness of the model, \mathbf{m}

$$F = \chi^2 + \mu |\mathbf{m}^T \partial^T \partial \mathbf{m}| \tag{1}$$

where ∂ is a second-derivative smoothing operator. Details regarding the inversion, including resolution tests, can be found in Laske et al. (2011). Formally, the optimal model minimizes sum F and is located in the corner of the trade-off curve between the two terms of F, but such models often tend to be unrealistically rough. For the phase velocity maps this means that high-amplitude anomalies may be placed in areas of poor path coverage. These anomalies tend to increase more rapidly than in well-covered areas as one moves along the trade-off curve toward rougher models. Another source of unrealistic anomalies may stem from internal inconsistencies in the data, which are often greater for longer periods than for shorter periods. We therefore choose slightly smoother models where such anomalies are muted but the data misfit is still within an acceptable limit, i.e. the normalized χ^2 remains close to 1. Our resulting maps yield realistic phase velocity

perturbations of several percent, for periods longer than 20 seconds. At shorter periods we allowed greater misfit reduction and greater model roughness (less smoothing) in order to produce results consistent with the level of variation in phase velocities expected by variations in both Earth structure and water depth.

At each OBS site, a 'local' phase velocity curve was constructed by sampling the phase velocity maps at the corresponding 1-degree cell. At each station, this curve was used together with the compliance curve as input data in the subsequent joint inversion for depth-dependent structure.

3 INVERSIONS FOR DEPTH-DEPENDENT STRUCTURE

3.1 Inversion for crustal and uppermost mantle structure

At each OBS site, we jointly inverted the seafloor compliance curve and the phase velocity curve for a 1-D shear velocity model by solving for deviations from a starting model and using a linearized Occam inversion (Constable et al. 1987). We used perturbation theory to link structural changes at depth to the frequency-dependent phase velocity. A small change in phase velocity at a specified period, c(T), can then be represented by the dot product of a sensitivity kernel (Fig. 3) with a small change in compressional and shear velocity, Vp and Vs, and density, ρ , integrated over depth, z,

$$\delta c(T) = \int_{0}^{z} \left(\tilde{K}_{P}(T, z) \cdot \delta V p(z) + \tilde{K}_{S}(T, z) \cdot \delta V s(z) + \tilde{K}_{R}(T, z) \cdot \delta \rho(z) \right) dz \tag{2}$$

where \tilde{K}_P , \tilde{K}_S , and \tilde{K}_R are the kernels for Vp, Vs and ρ , respectively. The linear representation above, or a simplification thereof, is routinely used in the analysis of surface wave dispersion for structure varying with depth (e.g., Romanowicz 2002; Laske & Widmer-Schnidrig 2015).

Perturbation theory applied to seafloor compliance will yield a similar set of equations. The kernels for a given model can be determined "semi-analytically" from the eigenfunctions of the wave equation. The "semi-analytically" here means that the eigenfunctions are still computed numerically either by integration over depth or a propagator matrix method. In this study, we determined the kernels chiefly numerically by perturbing the model at given depths and then evaluating the effects on the frequency-dependent phase velocity and seafloor compliance explicitly. The inverse of the linear system of equations described by equation (2) usually poses an underdetermined problem and leads to an ill-conditioned data kernel matrix that is difficult to invert. Researchers therefore often keep density and Vp fixed and invert only for Vs. We prefer to use empirical scaling relationship between Vs, Vp and density and collapse the inversion into one for Vs only, following the protocol described by Laske & Widmer-Schnidrig (2015), where factors of 1.7 and 2.5 scale kernels \tilde{K}_P and \tilde{K}_R to \tilde{K}_S . This allows Vp and density to vary with depth in the same way as Vs does.

Both Rayleigh wave phase velocity and seafloor compliance depend on structure in a non-linear fashion,

and the validity of perturbation theory depends on the starting model used to compute the kernels. For phase velocity, our experience has been that changes in structure of up to 10% or a few percent more can be treated with perturbation theory but changes on the order of 15% require a 'local' treatment where kernels should be recomputed with a new starting model. While the inversion of phase velocity is a well-used means to assess structure with depth, and the forward problem is discussed in many seismology textbooks (e.g., Udias 1999; Gubbins 1990; Stein & Wysession 2003), seafloor compliance is relatively rarely described, and the validity of pertubation theory has not been documented. In fact, this study may be the first one to combine both types of data. For clarity we juxtapose the two with the example of a homogeneous, halfspace medium. For such a medium Rayleigh wave phase velocity is found by solving Rayleigh's equation

$$\left(2 - \frac{c^2}{Vs^2}\right)^2 = 4\left(1 - \frac{c^2}{Vp^2}\right)^{1/2} \left(1 - \frac{c^2}{Vs^2}\right)^{1/2}$$

There is no dependence on density. Substitutions $\zeta=c^2/Vs^2$ and $\gamma=Vs^2/Vp^2$ ultimately yield a cubic equation for ζ (note a sign typo in Udias 1999)

$$\zeta^3 - 8\zeta^2 + 8\zeta(3 - 2\gamma) - 16(1 - \gamma) = 0 \tag{3}$$

For each value of $0 \le \gamma \le 1/2$ this equation has three roots but only those with $\zeta < 1$ (i.e. c < Vs) are valid for Rayleigh waves. For the simplified case of a Poisson solid ($\gamma = 1/3$), the only solution becomes $\zeta = 0.8453$, hence the phase velocity simply scales linearly with shear velocity as $c = \sqrt{0.8453}Vs$.

For a half-space, seafloor compliance, η , relates to structure as (Crawford 2004; Doran & Laske 2019)

$$\eta = \frac{Vp^2}{2\rho V s^2 (Vp^2 - Vs^2)} \tag{4}$$

Using the substitution above for γ , we obtain

$$\eta = \frac{1}{2\rho V s^2 (1 - \gamma)}$$

For a Poisson solid, this gives

$$\eta = \frac{3}{4\rho V s^2}$$

and so compliance scales with the inverse of $\rho V s^2$.

Given the more complex dependence of compliance to structure, even in a homogeneous half-space, we performed tests to assess how large structural variations may become before perturbation theory breaks down. This should provide more confidence that a joint inversion of seafloor compliance and phase velocity is reasonable. For this test, we predicted the compliance from two models as 'true' compliance. We then computed

kernels for the first model, treated the second model as perturbation to the first one and predicted compliance by multiplying the model perturbations with the kernels and integrating over depth. Finally, we compared the resulting 'perturbed' compliance with the original compliance for model 2. Such forward modeling indicated that deviations from the starting model can be approximated as linear perturbations as long as deviations are 10% or less in both Vp and Vs (Fig. 6). Using perturbation theory then, we related structure to compliance in a similar way as in equation (2). For both, phase velocity and compliance, we determined the kernels numerically using a starting model tailored for each OBS site individually. For the mantle, the same scaling factors as described above were used for both phase velocity and compliance. For the crust, the Vp/Vs ratio was forced to remain at 1.7 while density was not scaled.

At each station, we constructed the starting model using isotropic mantle velocities and density for oceanic lithosphere aged 52 - 110 Ma from Nishimura & Forsyth (1989) and the SWELL crustal model of Laske et al. (2007). There, the crystalline crust is represented by three layers, 2A, 2B and 3 with thicknesses 1.3, 2.0 and 3.0 km respectively. For the water layer, we adopted depth measurements taken during the OBS deployment cruises and a mean sound speed in the water column of 1500 m/s. The sediment structure, the primary controlling factor on seafloor compliance, was carefully constrained by Doran & Laske (2019). This initial model typically fit the compliance curves better than the phase velocity curves.

We inverted for perturbations to this starting model choosing five parameters: the shear velocity of the crust as well as the velocities of the top 40 km of the mantle, divided into four 10-km layers. So even though the crust is divided into 3 layers, we solved for a uniform perturbation across the three layers. The rationale behind this was two-fold: to limit the number of model parameters given the vertical resolution capabilities of the data; we assume that a process that alters relatively thin oceanic crust would affect the entire crystalline crust. To suppress artifacts in the resulting Vs models, we applied Occam regularization (see Laske et al. 2011, for details), where we imposed equal weights on the compliance and the dispersion data. The regularization parameter, μ , in equation (1) was kept at 10^{-4} . Crustal thickness, the sixth parameter, was solved for in an iterative fashion where we repeated the inversions by varying the crustal thickness between 6 and 25 km at 1 km intervals, thereby searching for the minimum misfit χ^2 . The purpose of this was to optimize the misfit trading off between crustal thickness and mantle velocities. While the Occam inversion will naturally do this, the large velocity jump between the crust and mantle occasionally led to an overly smooth model (ie, with no velocity jump) if the starting model was too far from the final model. For all crust thicker that 6.3 km, we assumed that the thickening was the result of magmatic underplating and introduced a 4th crustal layer in the starting model, where Vp = 7.3 km/s, Vs = 4.2 km/s (see Leahy et al. 2010) though we did not change the parameterization in the inversion, i.e. we still solved for a single perturbation to crustal velocities.

In the following, we discuss the results for two stations as examples. Phase velocities at PL57, far east

of the island of Hawaii, are slightly higher than predicted from the starting model (Fig. 7a). The inversion yielded higher velocities in the crust (1.3% above SWELL) and uppermost mantle just below the Moho discontinuity (1.5%), where deviations from the starting model decrease with increasing depth. The inversion reduced the misfit, χ^2 , of the phase velocity curve by 82% and reduced the compliance misfit by 22%. Phase velocities derived at PL24 just south of the island of Hawaii, on the other hand, were higher than predicted by the starting model at long periods but lower at short periods (Fig. 7b). The best fit to the phase velocities was found with elevated crustal (1.3%) and uppermost mantle (1.7%) velocities below the Moho, and with a 18 km thick crust. This model decreased the misfit of the phase velocities by 91% and the misfit of the compliance data by 22%. In both cases, the updated model resulted in lower misfit improvement to the compliance data because such data are primarily controlled by sedimentary structure, which was already accounted for. Note however that adjustments to crustal velocities improved the fit even for these data.

We repeated this analysis at 53 OBS stations in the array. At eight stations we obtained dispersion data but were unable to estimate compliance (PL06, PL18, PL21, PL32, PL61, PL63, PL67, PL68; see Table S1), typically because the seismometer was not sufficiently broadband (e.g., the Trillium T-40s), or due to issues with the DPG. Some seismometer records also exhibited long-period noise that did not affect ambient noise dispersion but inhibited the measurement of compliance. At these sites, we assumed sediment properties from Doran & Laske (2019), calculated from Ps delay times, and inverted only the phase velocities. We maintained a constant smoothing factor that was weighted towards smoother models. Our inversions yielded models of crustal thickness and velocity (Fig. 8) as well as mantle velocities in the uppermost 40 km (Fig. 9).

3.2 Model uncertainties and resolution

One measure of model uncertainty can be obtained by evaluating the final misfit χ^2 at each station (Fig. S2). Misfit from the joint inversion is highest to the immediate north of the island of Hawaii in the vicinity of the Molokai fracture zone and at station PL62 to the fast southeast. However, examining the final misfits alone may not fully characterize the model uncertainties. Although we derived dispersion at individual sites as input data in the final inversion, our two-station estimates of phase velocities are path-integrated measurements that represent structure between stations. Therefore, errors at a specific station may be introduced by structural artifacts or systematic errors at other stations. An additional source of uncertainty in our data modeling stems from variations in water depth. Bathymetric variations induce changes in phase velocities on the same order of magnitude as Earth structure, particularly at short periods (Figs. 4, S1). At each OBS site, water depths were determined by acoustic triangulation during deployment and should be accurate to within 100 meters or less (e.g., Russell et al. 2019). However, phase velocities sample structure within a diameter of more than

60 km (for periods of 16 seconds and longer), and compliance data are sensitive to structure within 10 km of a station (e.g., Hulme et al. 2005; Zha et al. 2014; Doran & Crawford 2020). As a cross-check to assess the potential contaminating effects of erroneous assumptions on water depth at each OBS site, we determined the median water depth within the corresponding 1° cell by averaged over the bathymetry map of Smith & Sandwell (1997). While the overall median difference between the two estimates was 105 meters, two stations (PL35 and PL36) showed differences of over 1000 meters. A difference in water depth of 2000 meters, as seen at PL36, can erroneously lead to a difference in inferred crustal thickness of 15 km. We therefore prefer to exclude these two stations from our final assessment of crustal thickness though they are included in the maps for shear velocity.

Trade-offs between model parameters introduce further modeling uncertainties. The compliance data act to constrain crustal velocities, but crustal thickness and mantle velocities are primarily constrained by the phase velocities. A thicker or slower crust can produce similar modeling misfit as a faster uppermost mantle. But changes in mantle velocity must remain small. For example, at PL06, for which we have only phase velocity data, our best-fitting model contains 11 km of crust (Fig. S3). A model with a 6-km thick crust as found by Leahy et al. (2010) fits our data nearly equally well, if the mantle velocity is reduced by 2.5%. A model with the original 11-km crust and a reduction of the mantle velocity by 3% fits some mid-period data better but increases the misfit overall. While this trade-off estimate of 5 km in crustal thickness and 2.5% in velocity variation appears large, we should note that the data are internally somewhat inconsistent thereby raising the difficulty to find a model that fits all data equally well. The data at both ends of the period range considered here are not in agreement with a model required by the rest of the data. The structure at station PL61 also is constrained only by phase velocity data but provides an example of internally more consistent data (Fig. S4). Here, a model with a 6-km crust now is accompanied by a mantle velocity reduction of only 1.5%. Since compliance data bear sensitivity to the crystalline crust, including such data in the inversion would further reduce this trade-off.

We attempted to quantify model uncertainties in a more comprehensive and quantitative manner using a Markov-chain Monte Carlo (MCMC) technique. In this approach, forward modeling is performed to more comprehensively sample the model space. We followed the general method as described by Ball et al. (2014) and Zha & Webb (2016). An i-th model, m_i , was obtained by perturbing a previous model m_{i-1} . The likelihood L(m) of the model was calculated as

$$L(m) = \exp\left(-\frac{1}{2}\left[c_1 \cdot \chi_{comp}^2 + c_2 \cdot \chi_{pv}^2 + c_3 \cdot \partial M\right]\right)$$
(5)

where χ_{comp} and χ_{pv} denote the misfits for compliance and phase velocity. The coefficients c_1 through c_3 were chosen to weigh tradeoffs between the individual misfits and the model smoothing. We set $c_1 = 4c_2$

and used similar smoothing weighting as done in the Occam inversion. The model m_i was accepted if the likelihood was greater than that of the previous model m_{i-1} . Models with lower likelihood were accepted with a probability of the ratio of the two likelihoods in order to distribute sampling the model space. We ran 5000 iterations of this algorithm at PL59 (Figs. 10, S8). The resulting median model shows similar characteristics as the one resulting from the Occam inversion, with higher velocities in the crust and mantle than the starting model. The uncertainty, calculated as the standard deviation in the histogram of accepted models, shows an average of 2% uncertainty at each depth. However, the median crustal thickness was 8 km, which is 2 km more than in the Occam model. Assuming the median value for each model parameter yielded a final dispersion curve with over twice the misfit as the Occam inversion. This suggests therefore that the MCMC process may yield a final model that is different from the one obtained in an Occam inversion, with a larger data misfit that is statistically significantly greater. Given the fact that the MCMC model has difficulties to fit the short-period phase velocities, we would give preference to the Occam model. But the MCMC proved useful to estimate model errors.

4 DISCUSSION & CONCLUSION

While the oceanic crystalline crust was found to be about 6 km at many of our OBS sites (28 out of 52), our results suggest that it can be up to 15 km on the Hawaiian Swell and up to 23 km closer to the Hawaiian Islands. This is in qualitative agreement with results of previous studies (e.g., Watts et al. 1985; ten Brink & Brocher 1987; Lindwall 1991; Leahy et al. 2010). In this analysis we refrained from interpreting data directly beneath the islands (i.e., land stations) as the 1-degree grid cells from our dispersion maps span over significant variations in topography, bathymetry, sedimentation, and short-scale crustal properties. In addition, land sites do not have collocated compliance data which hampers a direct comparison. Crustal velocities vary on the order of $\pm 3\%$. The crust exhibits lower seismic velocities immediately adjacent to the islands and downstream along the older seamounts, as might be expected in a region affected by melt, melt extraction, magmatic underplating (Leahy et al. 2010), high flexure (e.g., Watts & ten Brink 1989) or heavy sedimentation. We found a distinct region of anomalously thick crust to the immediate west of the island of Hawaii. This region includes a number of Cretaceous seamounts generally organized in a V-shape trending northeast, oblique to the trend of the Molokai Fracture Zone (Fornari & Campbell 1987). The South Arch volcanic field, only 1-10 ka in age, may also affect the regional crustal structure (e.g., Lipman et al. 1989; Bianco et al. 2005). Another distinct region of anomalous crust appears immediately to the southeast of Hawaii, potentially correlated with the leading edge of the proposed Hawaiian mantle plume (Wolfe et al. 2009). We did not observe evidence for systematic variations in crustal thickness as reported by ten Brink & Brocher (1988), but variations in layer 2A were not tightly constrained.

Our models display some disagreement with the crustal model of Leahy et al. (2010), which were derived from receiver functions assembled for PLUME land and OBS sites (Fig. S9). The crustal underplating they report is generally thinner and tightly confined to the island chain. Land-based seismic tomography also report crustal thicknesses near 15 km though such studies are often confined to the volcanically active region on the island of Hawaii (e.g. Tilmann et al. 2001; Lin et al. 2014). Two prominent exceptions in our comparison with Leahy et al. (2010) are sites PL07 and PL08 about 250 km northeast of the island of Hawaii and close to the Molokai Fracture Zone, where the authors reported crust over15 km in thickness, which we cannot reproduce. Thickness estimates from receiver functions may be biased high if thick sediments as found within the Hawaiian moat, but also at these two OBS sites (Doran & Laske 2019), are not accounted for. Similarly, sediment thickness at PL35, PL36 and PL47 is significant, which may have mapped into crustal thickness in the Leahy et al. (2010) study. Since the models presented here were 'informed' by the previous joint inversion of seafloor compliance and sediment converted phases (Doran & Laske 2019), the crustal thicknesses presented here should be less biased, especially since we also allowed for variations in crustal velocities.

On the other hand, our phase velocity estimates average over significant variation in bathymetry and resulting models may be less accurate in the vicinity of great bathymetric changes. We recall that stations PL35 and PL36 had the largest discrepancies between ship-based water depth estimates and those averaged over the bathymetry map. A similar averaging problem could explain why our crustal thickness estimate at PL02 just east of the island of Hawaii of 25 km is on the order of 5 km greater than that of Leahy et al. (2010), but the estimate at adjacent station PL01 is lower. Since crustal thickness estimates at stations PL36 and PL35 had large discrepancies between our initial estimates and that of Leahy et al. (2010), we performed additional targeted forward modeling for the phase velocities. At station PL35 (Fig. S5) we found that the initial crustal thickness of 6 km predicts phase velocities too high for most periods. A thicker crust of 11 km is much more consistent with the phase velocity data, except at a period of 16 s which we consider an outlier. Such a model would also fit the long-period compliance data much better. However, a 17-km thick crust, as proposed by Leahy et al. (2010), is incompatible with our phase velocity data. Fig. 8 therefore shows our best estimate of 11 km. At station PL36, the phase velocity data are internally inconsistent (Fig. S6) where the short-period phase velocity data require a thinner crust, but the long-period data are clearly best fit by a 17-km thick crust. Again the long-period compliance data would agree better with this thicker crust that is also proposed by Leahy et al. (2010). We therefore adopted this value as our final crustal thickness, even though the formal inversion initially yielded a 6-km thin crust. The situation at station PL47 is less obvious as the phase velocity curve exhibits some undulation where the short-period data are better matched by a thinner crust while some long-period data tend to be better fit by a thicker crust (Fig. S7). Here we adopted our original estimate of 6 km as the thicker crustal model that is proposed by Leahy et al. (2010) would significantly increase our data misfit.

In the uppermost mantle, we imaged a broad region of low velocities that generally trends east-west across the island chain. The velocity anomalies increase with increasing depth and are greatest at depths of 40 km. At least at shallower depth, the low velocities appear to cluster broadly along the Molokai Fracture Zone, whereas at 40 km depth, a pronounced low-velocity cluster appears just east of the island of Hawaii. This is in agreement with the findings of the long-period phase velocity study of Laske et al. (2011). Low velocities are typically interpreted as a result of elevated temperatures or melt content. Assuming no petrologic variations, upper mantle velocity anomalies of several percent could be consistent with excess temperatures on the order of 200°C and 2-3% melt fraction (Schmeling 1985; Goes et al. 2000; Kreutzmann et al. 2004; Laske et al. 2011) though these values apply to depths between 50 and 200 km depth. Taking only thermal effects into account and assuming a reset of the Hawaiian lithosphere from 80 Myr to 52 Myr, predictions by Faul & Jackson (2005) lead to a temperature decrease by about 100°C at 40 km depth, and a shear velocity decrease by 0.05 km/s, about 1.1%. The rest of the velocity anomaly could indicate melt of several percent. This would be in agreement with Tilmann et al. (2001) who observed low velocities beneath Hawaii at depths of 40 km and determined that temperature anomalies alone could not reproduce the result, instead attributing the effects to distributed melt networks. Focusing of melt from a distributed region into active conduits may therefore occur at depths between 20 - 40 km beneath Hawaii. The lithosphere-asthenosphere receiver function study of Rychert et al. (2013) inferred a 'restite root' directly beneath Hawaii. They speculate that a body composed of compositionally depleted but hot material was generated during the formation of the islands. The root is hypothesized to deflect melt west of the island in the asthenosphere and lower lithosphere. Such a root may contribute to lateral deflection of melt at shallower depths as well, pushing material eastward before it finally concentrates beneath Hawaii and travels to the surface.

Future plans for this work include a joint interpretation of our data with the receiver functions of Leahy et al. (2010). The latter provide additional, direct constraints on the total crustal thickness though we would probably have to allow for changes in scaling between Vp and Vs, which adds complexity to the modeling process. A modification to the model parameterization would be to allow the oceanic crust (the upper 6.3 km) and the underplated part to vary independently. Most likely, this would improve the fit to our data, not lastly because the model vector would be larger. But the fit could also be improved as compliance data that are more sensitive to the upper crust may require different changes in Vs than the phase velocities that are more sensitive to the lower crust and uppermost mantle. Here then, a more in-depth comparison between the

results of a classical Occam inversion and a MCMC approach, or even a transdimensional approach where we would also allow the number of model parameters to vary may become insightful and necessary.

ACKNOWLEDGMENTS

PLUME waveforms and station metadata are publically available and were accessed through the Incorporated Research Institutions for Seismology Data Management Center (IRIS DMC;

http://ds.iris.edu/ds/nodes/dmc/). The data were accessed between November 2016 and June 2017 to compute compliance data and were accessed between April and June 2018 to calculate ambient noise cross-correlation waveforms. Some data processing was performed using the Python toolbox ObsPy (Krischer et al. 2015). Figures were created using Generic Mapping Tools (Wessel et al. 2013). Dispersion forward modeling was performed using the algorithms of Haney & Tsai (2017). This research was supported by NSF grant OCE-1736516.

REFERENCES

- Agius, M. R., Rychert, C.A., Harmon, N. & Laske, G., 2017. Mapping the mantle transition zone beneath Hawaii from Ps receiver functions: Evidence for a hot plume and cold mantle downwellings. *Earth Planet. Sci. Lett.*, **474**, 226–236, doi:10.1016/j.epsl.2017.06.033.
- Aki, K., 1957. Space and time spectra of stationary waves with special reference to microtremors. *Bull. Earthq. Res. Inst.*, **35**, 415 457.
- Ball, J. S., Sheehan, A. F., Stachnik, J. C., Lin, F.-C. & Collins, J. A., 2014. A joint Monte Carlo analysis of seafloor compliance, Rayleigh wave dispersion and receiver functions at ocean bottom seismic stations offshore New Zealand. *Geochem. Geophys. Geosyst.*, **15**, 5051–5068, doi:10.1002/2014GC005412.
- Bell, S. W., Forsyth, D. W. & Ruan, Y., 2015. Removing noise from the vertical component records of ocean-bottom seismometers: Results from year one of the Cascadia Initiative. *Bull. seism. Soc. Am.*, **105**, 300–313, doi:10.1785/0120140054.
- Bensen, G. D., Ritzwoller, M. H., Barmin, M. P., Levshin, A. L., Lin, F., Moschetti, M. P., Shapiro, N. M. & Yang, Y., 2007. Processing seismic ambient noise data to obtain reliable broad-band surface wave dispersion measurements. *Geophys. J Int.*, **169**, 1239–1260, doi: 10.1111/j.1365–246X.2007.03374.x.
- Bianco, T. A., Ito, G., Becker, J. M. & Garcia, M. O., 2005. Secondary Hawaiian volcanism formed by flexural arch decompression. *Geochem. Geophys. Geosyst.*, **6**, Q08009, doi:10.1029/2005GC000945.
- Campillo, M. & Roux, P., 2015. Crust and Lithospheric Structure Seismic Imaging and Monitoring with Ambient Noise Correlations. in: Gerald Schubert (editor-in-chief) *Treatise on Geophysics*, 2nd edition, Vol 1. Oxford: Elsevier, 391–417.

- Cheng, C., Allen, R.M., Porritt, R.W. & Ballmer, M.D., 2015. Hawaiian Volcanoes: From Source to Surface, chap. Seismic constraints on a double-layered asymmetric whole-mantle plume beneath Hawai'i. in: R. Carey, V. Cayol, M. Poland & D. Weis (eds) *Hawaiian Volcanoes: from source to surface, Geophys. Monograph. Ser.*, 208, 19–34, doi:10.1002/9781118872079.ch2.
- Collins, J. A., Wolfe, C. J., & Laske, G., 2012. Shear wave splitting at the Hawaiian hot spot from the plume land and ocean bottom seismometer deployments. *Geochem. Geophys. Geosyst.*, **13**, Q02007, doi:10.1029/2011GC003881.
- Constable, S. & Heinson, G., 2015. Hawaiian hot-spot swell structure from seafloor MT sounding. *Tectonophysics*, **389**, 111–124, doi: 10.1016/j.tecto.2004.07.060.
- Constable, S. C., Parker, R. L. & Constable, C. G., 1987. Occam's inversion: A practical algorithm for generating smooth models from electromagnetic sounding data. *Geophysics*, **52**, 289–300, doi:10.1190/1.1442303.
- Cox, C., Deaton, T. & Webb, S., 1984. A deep-sea differential pressure gauge. J. Atmos. Oceanic Technol., 1, 237–246.
- Crawford, W. C., 2004. The sensitivity of seafloor compliance measurements to sub-basalt sediments. *Geophys. J Int.*, **157**, 1130–1145, doi: 10.1111/j.1365-246X.2004.02264.x.
- Crawford, W. C. & Webb, S. C., 2002. Variations in the distribution of magma in the lower crust and at the Moho beneath the East Pacific Rise at 9° 10° N. *Earth Planet. Sci. Lett.*, **203**, 117–130.
- Crawford, W. C., Webb, S. C., & Hildebrand, J. A., 1991. Seafloor compliance observed by long-period pressure and displacement measurements. *J. geophys. Res.*, **96(B10)**, 16,151–16,160, doi:10.1029/91JB01577.
- Crawford, W. C., Stephen, R. A., & Bolmer, S. T., 2006. A second look at low-frequency marine vertical seismometer data quality at the OSN-1 site off Hawaii for seafloor, buried, and borehole emplacements. *Bull. seism. Soc. Am.*, **96**, 1952–1960, doi:10.1785/0120050234.
- Doran, A. K. & Crawford, W.C., 2020. Continuous evolution of oceanic crustal structure following an eruption at Axial Seamount, Juan de Fuca Ridge. *Geology*, **48**, doi:10.1130/G46831.1.
- Doran, A. K. & Laske, G., 2016. Infragravity waves and horizontal seafloor compliance. *J. geophys. Res.*, 121, 260–278, doi:10.1002/2015JB012511.
- Doran, A. K. & Laske, G., 2017. Ocean-bottom seismometer instrument orientations via automated Rayleigh-wave arrival angle measurements. *Bull. seism. Soc. Am.*, **107(2)**, 691–708, doi:10.1785/012016165.
- Doran, A. K. & Laske, G., 2019. Seismic structure of marine sediments and upper oceanic crust surrounding Hawaii. *J. geophys. Res.*, **124**, 2038–2056, doi:10.1029/2018JB016548.
- Doran, A. K., Rapa, M., Laske, G., Babcock, J. & McPeak, S., 2019. Calibration of differential pressure gauges through in situ testing. *Earth Space Sci.*, **6**, 2663–2670, doi:10.1029/2019EA000783.
- Ekström, G., Abers, G.A. & Webb, S. C., 2009. Determination of surface-wave phase velocities across USArray from noise and Aki's spectral formulation. *Geophys. Res. Lett.*, **36**, L18301, doi:10.1029/2009GL039131.
- Faul, U. H., & Jackson, I., 2005. The seismological signature of temperature and grain size variations in the upper mantle. *Earth Planet. Sci. Lett.*, **234**, 119–134, doi:10.1016/j.epsl.2005.02.008.
- Fornari, D. J., & Campbell, J.F., 1987. Submarine topography around the Hawaiian Islands. in: R. W. Decker, T. L. Wright & P. H. Stauffer (eds.) *Volcanism in Hawaii*, US Geological Survey Professional Paper 1350, 109–124.

- French, S. W.& Romanowicz, B., 2015. Broad plumes rooted at the base of the Earth's mantle beneath major hotspots. *Nature*, **525**, 95–99, doi:10.1038/nature14876.
- Goes, S., Govers, R. & Vacher, P., 2000. Shallow mantle temperatures under Europe from P and S wave tomography. J. geophys. Res., 105(B5), 11,153 - 11,169, doi:10.1029/1999JB900300.
- Gubbins, D., 1990. Seismology and Plate Tectonics. Cambridge Univ. Press, Cambridge, UK, 339pp.
- Haney, M.M.& Tsai, V. C., 2017. Perturbational and nonperturbational inversion of Rayleigh-wave velocities. *Geophysics*, **82:3**, F15 F28, doi: 10.1190/geo2016-0397.1.
- Harmon, N., Forsyth, D. & Webb, S., 2007. Using ambient seismic noise to determine short- period phase velocities and shallow shear velocities in young oceanic lithosphere. *Bull. seism. Soc. Am.*, **97**, 2009–2023, doi: 10.1785/0120070050.
- Hulme, T., Crawford, W. C. & Singh, S. C., 2005. The sensitivity of seafloor compliance to two-dimensional low-velocity anomalies. *Geophys. J Int.*, **163**, 547–558, doi:10.1111/j.1365–246X.2005.02753.x.
- Kreutzmann, A., Schmeling, H., Junge, A., Ruedas, T., Marquart, G. & Bjarnason, I. Th., 2004. Temperature and melting of a ridge-centered plume with applications to Iceland. Part II: predictions for electromagnetic and seismic observables. *Geophys. J Int.*, , **159**, 1097–1111.
- Krischer, L., Megies, T., Barsch, R., Beyreuther, M., Lecocq, T., Caudron, C. & Wassermann, J., 2015. ObsPy: a bridge for seismology into the scientific Python ecosystem. *Comput. Sci. Disc.*, **8**, 014003, doi: 10.1088/1749-4699/8/1/014003.
- Laske, G.& Widmer-Schnidrig, R., 2015. Theory and Observations: Normal Mode and Surface Wave Observations. in: Gerald Schubert (editor-in-chief) *Treatise on Geophysics*, 2nd edition, Vol 1. Oxford: Elsevier, 117–167, doi:10.1016/B978-0-444-53802-4.00003-8.
- Laske, G., Phipps Morgan, J. & Orcutt, J. A., 2007. The Hawaiian SWELL pilot experiment Evidence for lithosphere rejuvenation from ocean bottom surface wave data. in: G.R. Foulger and D.M. Jurdy (eds.) *Plates, plumes, and planetary processes: Geological Society of America, Special Paper 430*, 209–233, doi:10.1130/2007.2430(11).
- Laske, G., Collins, J. A., Wolfe, C. J., Solomon, S. C., Detrick, R. S., Orcutt, J. A., Bercovici, D. & Hauri, E. H., 2009. Probing the Hawaiian hot spot with new ocean bottom instruments. *Eos Trans. AGU*, **90**(41, 362–363, doi: 10.1029/2009EO410002.
- Laske, G., Markee, A., Orcutt, J. A., Wolfe, C. J., Collins, J.A., Solomon, S. C., Detrick, R. S., Bercovici, D. & Hauri, E. H., 2011. Asymmetric shallow mantle structure beneath the Hawaiian Swell evidence from Rayleigh waves recorded by the PLUME network. *Geophys. J Int.*, **187**, 1725–1742, doi:10.1111/j.1365-246X.2011.05238.x.
- Leahy, G. M. & Park, J., 2005. Hunting for oceanic island Moho. *Geophys. J Int.*, **160**, 1020–1026, doi:10.1111/j.1365-246X.2005.02562.x.
- Leahy, G., Collins, J. A., Wolfe, C. J., Laske, G. & Solomon, S. C., 2010. Underplating of the Hawaiian Swell: Evidence from teleseismic receiver functions. *Geophys. J Int.*, **183**, 313–329, doi:10.1111/j.1365-246X.2010.04720.x.
- Lecocq, T., Caudron, C. & Brenguier, F., 2014. MSNoise, a Python package for monitoring seismic velocity changes using ambient seismic noise. *Seimol. Res. Lett.*, **85**, 715 726, doi: 10.1785/0220130073.

- Leslie, S. C., Moore, G. F., Morgan, J. K. & Hills, D. J., 2002. Seismic stratigraphy of the Frontal Hawaiian Moat: implications for sedimentary processes at the leading edge of an oceanic hotspot trace. *Marine Geol.*, **184**, 143–162, doi:10.1016/S0025-3227(01)00284-5.
- Li, X., Kind, R., Yuan, X., Wölbern, I. & Hanka, W., 2004. Rejuvenation of the lithosphere by the Hawaiian plume. *Nature*, **427**, 827–829.
- Lin, F.-C., Ritzwoller, M. H. & Shapiro, N. M., 2006. Is ambient noise tomography across ocean basins possible. *Geophys. Res. Lett.*, **33**, L14304, doi: 10.1029/2006GL026610.
- Lin, G., Shearer, P.M., Matoza, R.S., Okubo, P.G. & Amelung, F., 2014. Three-dimensional seismic velocity structure of Mauna Loa and Kilauea volcanoes in Hawaii from local seismic tomography. *J. geophys. Res.*, **119**, 4377–4392, doi: 10.1002/2013JB010820.
- Lindwall, D. A., 1991. Old Pacific crust near Hawaii: A seismic view. *J. geophys. Res.*, **96(B5)**, 8191–8203, doi:10.1029/91JB00149.
- Lipman, P. W., Clague, D. A., Moore, J. G. & Holcomb, R.T., 1989. South Arch volcanic field Newly identified young lava flows on the sea floor south of the Hawaiian Ridge. *Geology*, **17**, 611 614.
- Marone, F. & Romanowicz, B., 2007. Non-linear crustal corrections in high-resolution regional waveform seismic tomography. *Geophys. J Int.*, **170**, 460–467, doi: 10.1111/j.1365–246X.2007.03399.x.
- Matthews, K. J., Müller, R. D., Wessel, P. & Whittaker, J. M., 2011. The tectonic fabric of the ocean basins. *J. geophys. Res.*, **116**, B12109, doi:10.1029/2011JB008413.
- Morgan, J., 1971. Convection plumes in the lower mantle. *Nature*, **230**, 42 43.
- Müller, R. D., Sdrolias, M., Gaina, C. & Roest, W. R., 2008. Age, spreading rates and spreading symmetry of the world's ocean crust. *Geochem. Geophys. Geosyst.*, **9**, G04006, doi:10.1029/2007GC001743.
- Nishimura, C. E. & Forsyth, D. W., 1989. The anisotropic structure of the upper mantle in the Pacific. *Geophys. J Int.*, **96**, 203–229, doi:10.1111/j.1365-246X.1989.tb04446.x.
- Phipps Morgan, J., Morgan, W.J., & Price, E.. Hotspot melting generates both hotspot volcanism and a hotspot swell? *J. geophys. Res.*, **100**(**B5**), 8045–8062, doi:10.1029/94JB02887.
- Rees, B. A., Detrick, R. S. & Coakley, B. J., 1993. Seismic stratigraphy of the Hawaiian flexural moat. *Geol. Soc. Am. Bull.*, **105**, 189–205.
- Ritsema, J., & Allen, R. M., 2003. The elusive mantle plume. *Earth Planet. Sci. Lett.*, **207**, 1–12, doi:10.1016/S0012-821X(02)01093-2.
- Romanowicz, B., 2002. Inversion of surface waves: A review. in: W. H. K. Lee, H. Kanamori, P. C. Jennings, & C. Kisslinger, (eds)*International Handbook of Earthquake Engineering Seismology, Volume 81A*, Academic Press 149–173, doi:10.1016/S0074-6142(02)80214-5.
- Russell, J. B., Eilon, Z. & Mosher, S.G., 2019. OBSrange: A new tool for the precise remote location of ocean-bottom seismometers. *Seimol. Res. Lett.*, **90**, 1627 1641, doi:10.1785/0220180336.
- Rychert, C.A., Laske, G., Harmon, N. & Shearer, P. M., 2013. Seismic imaging of melt in a displaced Hawaiian plume. *Nature Geoscience*, **6**, 657–660, doi:10.1038/ngeo1878.

- Schmeling, H., 1985. Numerical models on the influence of partial melt on elastic, anelastic and electric properties of rocks. Part I: elasticity and anelasticity. *Phys. Earth Planet. Inter.*, **41**, 34 57, doi:10.1016/0031-9201(85)90100-1.
- Smith, W. H. F. & Sandwell, D. T., 1997. Global sea floor topography from satellite altimetry and ship depth soundings. *Science*, **277**, 1956–1962, doi:10.1126/science.277.5334.1956.
- Stein, S. & Wysession, M., 2003. An Introduction to Seismology, Earthquakes and Earth Structure. Blackwell Publishing, Oxford, UK, 498pp.
- ten Brink, U. S., & Brocher, T. M., 1987. Multichannel seismic evidence for a subcrustal intrusive complex under Oahu and a model for Hawaiian volcanism. *J. geophys. Res.*, **92(B13)**, 13,687–13,707, doi:10.1029/JB092iB13p13687.
- ten Brink, U. S., & Brocher, T. M., 1988. Multichannel seismic evidence for variations in crustal thickness along the Molokai Fracture Zone in the Mid-Pacific. *J. geophys. Res.*, **93(B2)**, 1119–1130, doi:10.1029/JB093iB02p01119.
- Tilmann, F. J., Benz, H. M., Priestley, K. F. & Okubo, P.G., 2001. P-wave velocity structure of the uppermost mantle beneath Hawaii from traveltime tomography. *Geophys. J Int.*, **146**, 594–606, doi:10.1046/j.1365-246X.2001.00480.x.
- Udias, A., 1999. Principles of Seismology. Cambridge Univ. Press, Cambridge, UK, 475pp.
- Watts, A. B., ten Brink, U. S., Buhl, P. & Brocher, T. M., 1985. A multichannel seismic study of lithospheric flexure across the Hawaiian–Emperor seamount chain. *Nature*, **315**, 105–111, doi:10.1038/315105a0.
- Watts, A. B. & ten Brink, U. S., 1989. Crustal structure, flexure, and subsidence history of the Hawaiian Islands. *J. geophys. Res.*, **94**, 10,473 10,500, doi:10.1029/JB094iB08p10473.
- Wessel, P., Smith, W. H. F., Scharroo, R., Luis, J. & Wobbe F., 2013. Generic mapping tools: Improved version released. *Eos Trans. AGU*, **94**, 409–410, doi:10.1002/2013EO450001.
- Wilson, J. T., 1963. A possible origin of the Hawaiian islands. Can. J. Phys., 41, 863–870, doi:10.1139/p63-094.
- Wölbern, I., Jacob, A. W. B., Blake, T. A., Kind, R., Li, X., Yuan, X., Duennebier, F. & Weber, M., 2006. Deep origin of the Hawaii tilted plume conduit derived from receiver functions. *Geophys. J Int.*, **166**, 767 781, doi: 10.1111/j.1365–246X.2006.03036.x.
- Wolfe, C. J., Solomon, S. C., Laske, G., Collins, J. A., Detrick, R. S., Orcutt, J. A., Bercovici, D. & Hauri, E. H., 2009. Mantle shear-wave velocity structure beneath the Hawaiian hot spot. *Science*, **326**, 1388–1390, doi:10.1126/science.1180165.
- Wolfe, C. J., Solomon, S. C., Laske, G., Collins, J. A., Detrick, R. S., Orcutt, J. A., Bercovici, D. & Hauri, E. H., 2011. Mantle *P*-wave velocity structure beneath the Hawaiian hotspot. *Earth Planet. Sci. Lett.*, **303**, 267–280, doi: 10.1016/j.epsl.2011.01.004.
- Zha, Y. & Webb, S. C., 2016. Crustal shear velocity structure in the Southern Lau Basin constrained by seafloor compliance. *J. geophys. Res.*, 121, 3220–3237, doi: 10.1002/2015JB012688.
- Zha, Y., Webb, S. C., Nooner, S. L. & Crawford, W. C., 2014. Spatial distribution and temporal evolution of crustal melt distribution beneath the East Pacific Rise at 9°–10°N inferred from 3-D seafloor compliance modeling. *J. geophys. Res.*, **119**, 4517–4537, doi:10.1002/2014JB011131.
- Zucca, J. J., Hill, D.P. & Kovach, R.L., 1982. Crustal structure of Mauna Loa Volcano, Hawaii, from seismic refraction and gravity data. *Bull. seism. Soc. Am.*, **72**, 1535–1550.

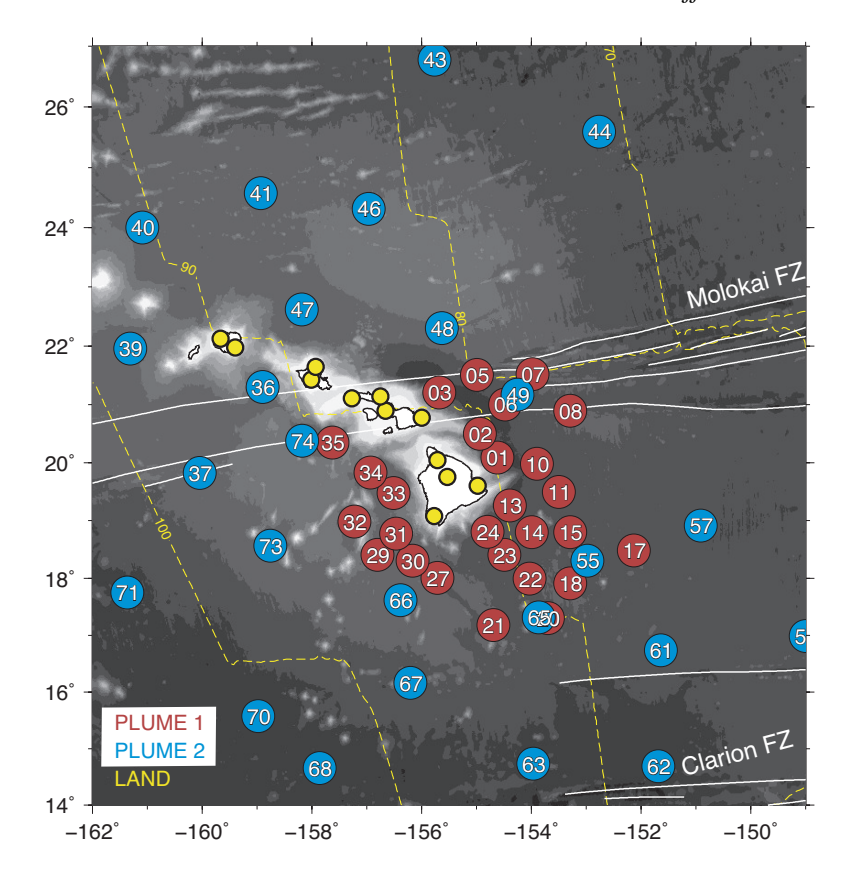


Figure 1. Location map for PLUME seismometers used in this study. Phase 1 OBSs are shown in red, Phase 2 OBSs are shown in blue, and land stations are shown in yellow. OBSs are labeled with station identification numbers for reference. Seafloor ages from Müller et al. (2008) are shown in 10 Ma intervals with dashed yellow lines. Bathymetry was taken from Smith & Sandwell (1997). Estimated traces of the Molokai and Clarion Fracture Zones as presented by Matthews et al. (2011) are shown in white.

This paper has been produced using the Blackwell Scientific Publications GJI LATEX2e class file.

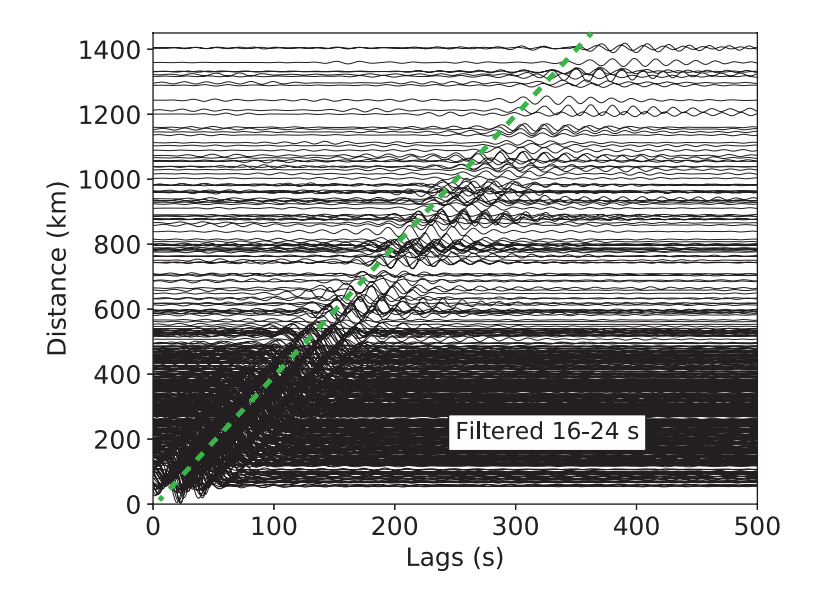


Figure 2. Stacked cross-correlation waveforms for all two-station pairs that produced usable phase velocity estimates (484 pairs). The stacks are sorted by inter-station distance. The waveforms were bandpass filtered between 16 and 24 seconds. The green dashed line denotes the travel time for a phase velocity of 4.0 km/s that is expected for 20-s Rayleigh waves traveling in a 5 km deep ocean near Hawaii (with 200 m of sediments; SWELL model from Laske et al., 2007).

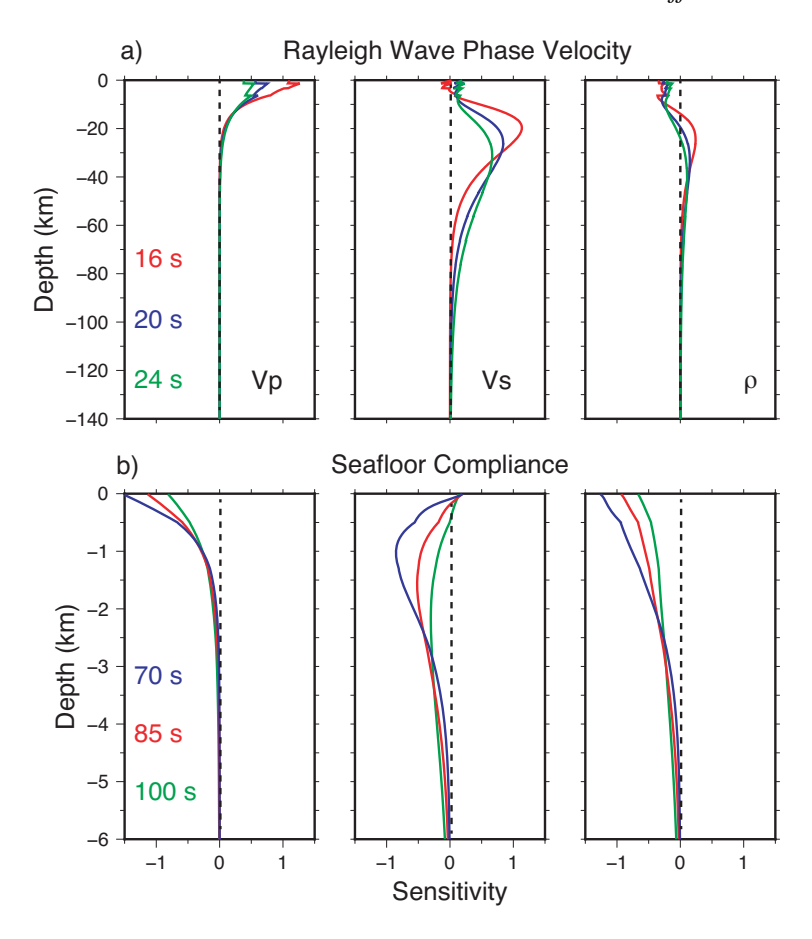


Figure 3. Sensitivity kernels for Rayleigh wave phase velocity (a) and seafloor compliance (b) to perturbational changes in compressional and shear velocities, Vp and Vs, and density, ρ , as function of depth. Different colors represent three periods for each data type relevant to this study. The underlying model, as described in the text, has a water depth of 5000 meters and no sediments. The kernels indicate that higher Vp or Vs yield higher phase velocities. On the other hand, higher Vp or Vs yield lower compliance values. The kernels for density generally trace those for Vs in the case of phase velocity, but those for Vp in the case of compliance.

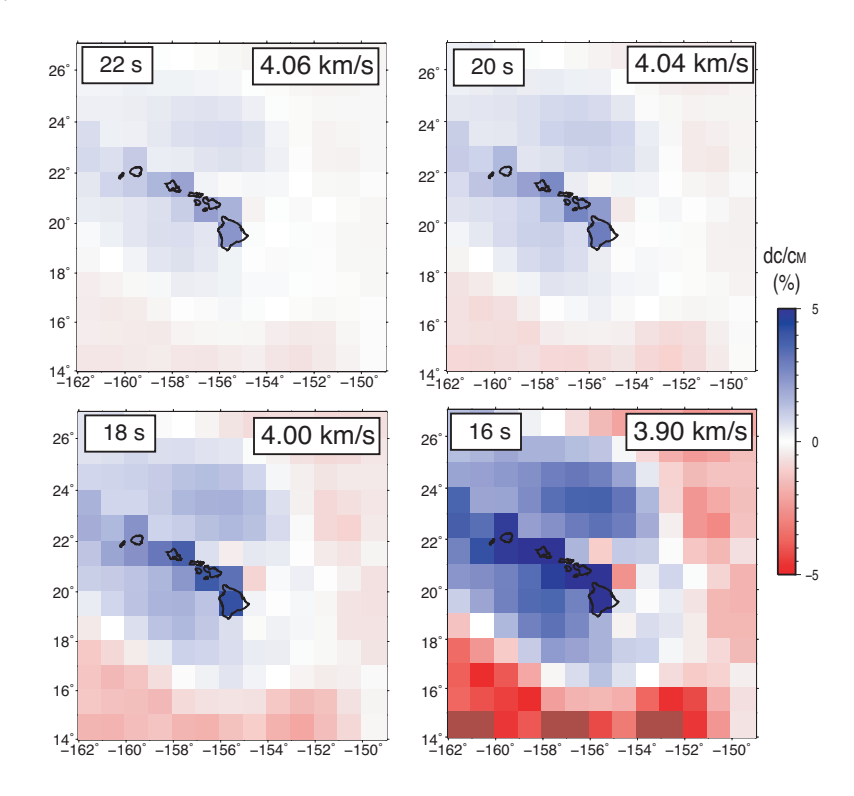


Figure 4. The effects on Rayleigh wave phase velocity from the bathymetry around Hawaii, averaged over 1-degree cells, and shown as percentage perturbation to the median velocity, c_M (upper right corner in each panel). Shown are effects for four periods relevant to this study (upper left corner). The average water depth in each cell was determined from the bathymetry map of Smith & Sandwell (1997). The solid earth structure used in each grid cell is identical.

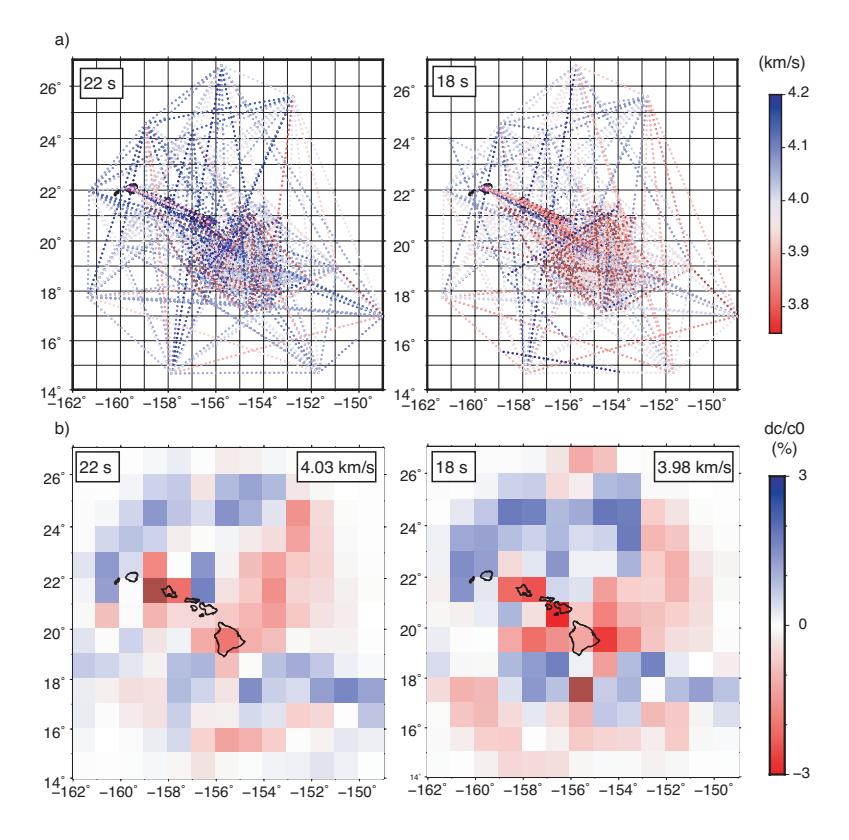


Figure 5. a) Measured path-averaged phase velocities for two-station pairs at periods of 22 (left) and 18 seconds (right). OBS – OBS, OBS – land, and land – land paths were considered.

b) Phase velocity maps parameterized in 1° cells resulting from tomographic inversions of the path-averaged dispersion curves shown above. Velocities are shown as a percentage deviation from a reference value, c_0 (upper right box in each panel).

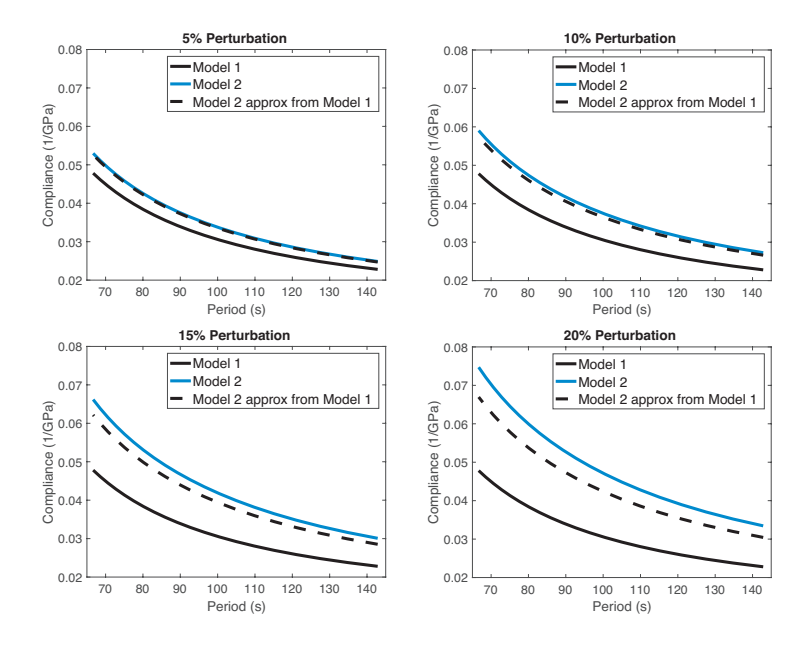


Figure 6. Test of perturbation theory with seafloor compliance data using 2 models. Model 1 is fixed while the velocity in the sediment layer in model 2 differs increasingly for each panel (5, 10, 15, 20%). The curves shown are predictions using the exact theory for both models (solid line) and when model 2 is treated as perturbation to model 1 (dashed line). At perturbations of 15%, predictions using perturbation theory start to divert markedly from the predictions using the exact theory.

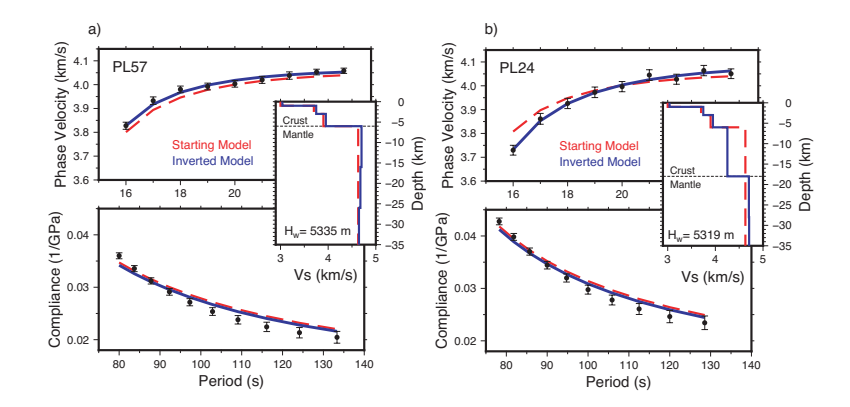


Figure 7. Inversion results at two individual stations: PL57 (a) and PL24 (b). The two larger panels show the fit of the starting (red) and final (blue) models to the phase velocity (upper panel) and compliance (lower panel). The insets show Vs models as a function of depth. The starting models, corrected for bathymetry (H_W), have 6 km of crystalline crust and typical mantle velocities. The sediment thicknesses at the stations are 106 and 72 m, respectively (see Doran and Laske, 2019).

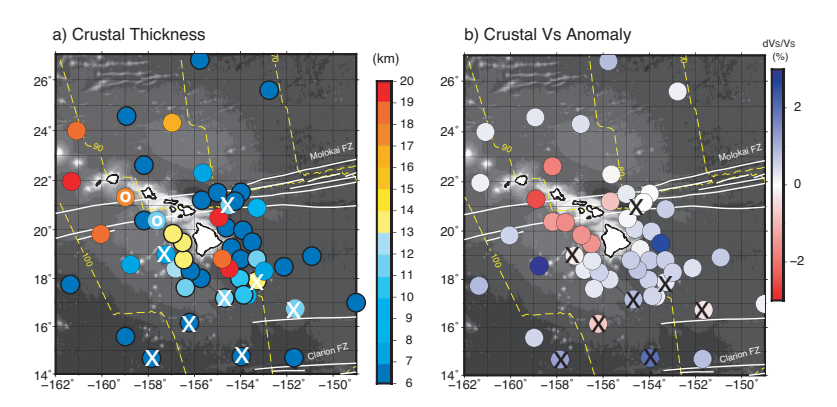


Figure 8. a) Final model for crystalline crustal thickness at the PLUME OBS sites surrounding the Hawaiian islands, after joint inversion of compliance and Rayleigh wave phase velocity. The crust is thickest at PL02 (23 km) and PL23 (21 km) (see Table S1). White circles mark two stations, PL35 and PL36 for which bathymetry changes quickly and inferred crustal thickness may be uncertain. b) Perturbations to crustal shear velocities, Vs, in the three-layer crystalline crust. Stations for which the OBS deployment depth and averaged bathymetry in the corresponding 1°cell differed by over 1000 meters were excluded. 'X' symbols mark eight stations for which only phase velocity data were used in the inversion.

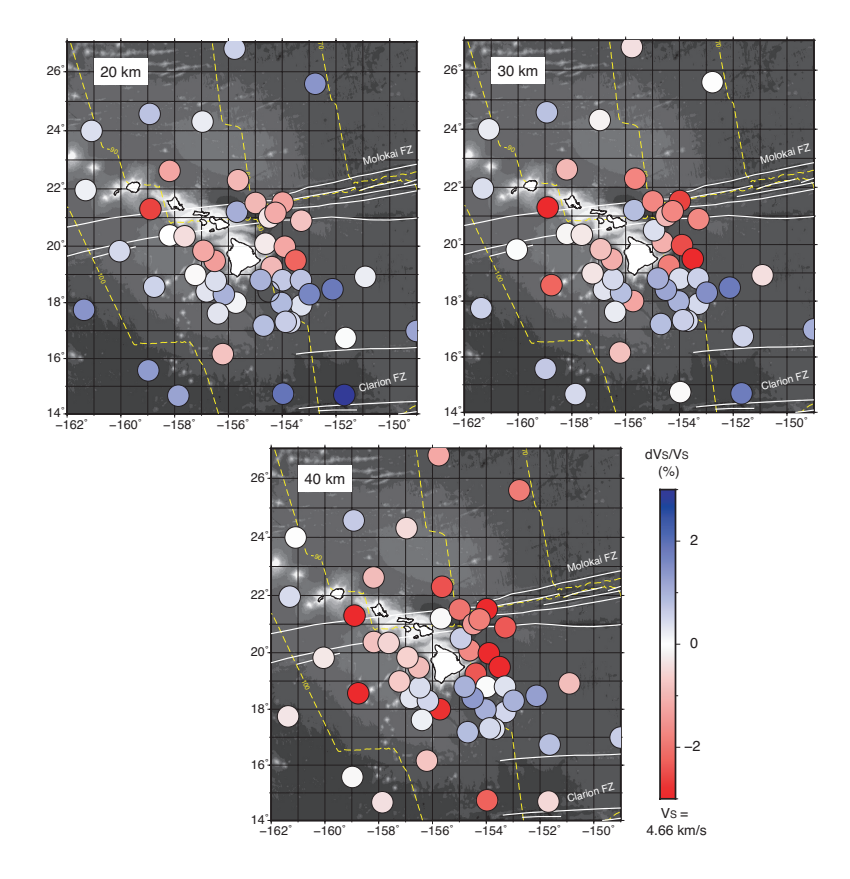


Figure 9. Shear velocities for the uppermost mantle at depths of 20, 30, and 40 km. Velocities are shown as a percentage perturbation to the reference velocity (Vs=4.66 km/s).

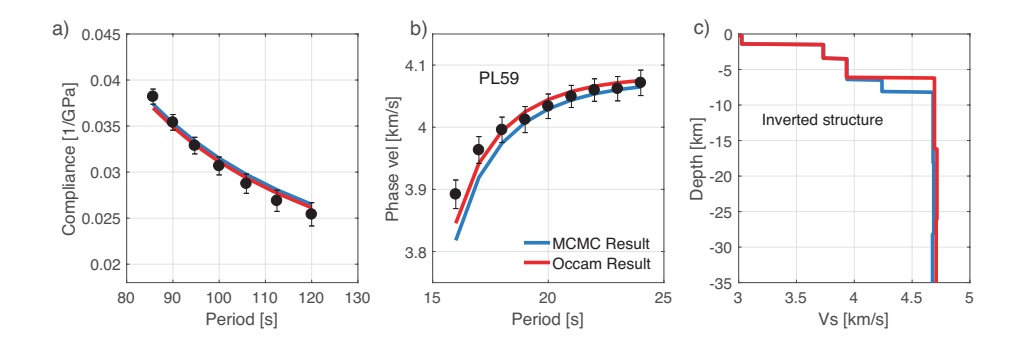


Figure 10. Fit to OBS site PL59 compliance (a) and phase velocity (b) by the final models (c) using the classical Occam inversion (red) and the Markov-Chain Monte Carlo approach (blue). The data misfit is greater for the MCMC model.